Design of Wireless Links to Implanted Brain–Machine Interface Microelectronic Systems

Toni Björninen, *Member, IEEE*, Rikky Muller, *Student Member, IEEE*, Peter Ledochowitsch, *Student Member, IEEE*, Lauri Sydänheimo, *Member, IEEE*, Leena Ukkonen, *Member, IEEE*, Michel M. Maharbiz, *Senior Member, IEEE*, and Jan M. Rabaey, *Fellow, IEEE*

***Abstract*—This letter presents a monolithic integration of an antenna with an array of neural recording electrodes on a flexible thin film. The structure was designed for long-term neural recording in a wireless brain-machine interface system. The implant–on-body antenna pair is optimized for maximal link power efficiency to maximize the battery life of a portable outside-body control unit. We provide guidelines for the design of the sub-skin-depth implant antenna and validate the antenna simulation model with wireless link measurements in air. We propose a new computational analysis of both the power and voltage delivery to the battery-free implant under design variations to guarantee efficient on-chip RF-to-dc conversion.**

***Index Terms*—Electrocorticography (ECoG), implantable antenna, on-body antenna, thin conductor, wireless power delivery.**

I. Introduction

RECENT advances in the field of brain–machine interfaces (BMIs) have caught wide attention in engineering and medicine. However, any transcranial wired readout of neural activity poses a high infection risk and is hence only fit for short-term clinical use. Battery-assisted wireless systems require perilous and expensive surgeries for replacing the discharged batteries. Thus, achieving fully wireless and battery-free operation is presently a major focus in the research on BMI hardware. In the future, wireless BMI systems fit for long-term neural recordings during patients' normal activities may aid diagnosing of diseases, such as epilepsy, sleep disorders, and mental disorders. Moreover, this technology holds the promise to restore mobility and communication for patients suffering from spinal cord injuries and neurodegenerative diseases by enabling direct brain-control of prosthetics [1], [2].

This letter focuses on characterizing and optimizing a wireless link to a battery-free BMI microelectronic system based on electrocorticography (ECoG), a neural recording technique where an array of electrodes is placed on the surface of the cerebral cortex to record the aggregate electrical activity of postsynaptic potentials generated by ensembles of cortical neurons [3]. The proposed system shown in Fig. 1 is comprised of a high-density microfabricated ECoG grid and a loop antenna bonded to an integrated circuit, which performs signal acquisition, wireless power delivery and communication.

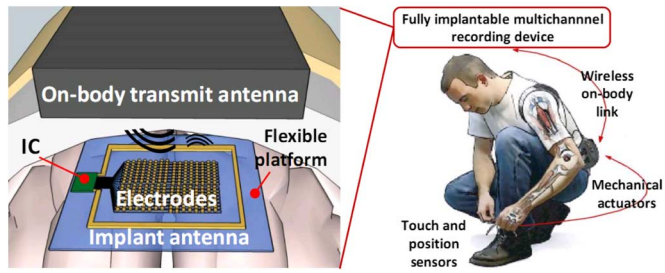

Fig. 1. System concept (illustration on the right from [1]).

State-of-the-art work on implantable antennas for BMIs has been focused on antenna miniaturization [4], [5] in order to minimize tissue scarring and immune response to the implant. However, this extreme miniaturization has been at the expense of link power efficiency, which drops sharply as the implant size is reduced below a few millimeters [6]. The proposed antenna is micropatterned onto a polymer thin film together with the ECoG electrodes, thus enabling a larger antenna size while eliminating the need to implant a large rigid structure. The nanoscale thickness of the metallization allows the entire structure to be flexible and conformal.

To our knowledge, this is the first monolithic integration of a sub-skin-depth-thin antenna with an ECoG grid on wafer level. In this letter, we provide antenna design guidelines for this challenging scenario. We present a cohesive computational approach to analyze both the power and voltage delivery to the implant under design variations to guarantee efficient and reliable on-chip RF-to-dc conversion.

II. System Requirements and Design Constraints

Frequencies ranging from hundreds of megahertz to low gigahertz have been found suitable for powering and communicating with implanted millimeter-sized biomedical systems [4]. Modulation of the impedance terminating the implant antenna (similar to radio frequency identification tags) provides superior power efficiency on the implant side [6]. This enables the battery-free operation for long-term neural recording [5]–[8].

Manuscript received December 13, 2012; accepted January 07, 2013. Date of publication January 11, 2013; date of current version January 31, 2013. This work was funded by Academy of Finland and Finnish Technology Industries and Sponsors of Berkeley Wireless Research Center.

T. Björninen, L. Sydänheimo, and L. Ukkonen are with the Department of Electronics and Communications Engineering, Tampere University of Technology, Tampere 33101, Finland (e-mail: toni.bjorninen@tut.fi).

R. Muller and J. M. Rabaey are with the Berkeley Wireless Research Center, University of California, Berkeley, Berkeley, CA 94704 USA (e-mail: rikky@eecs.berkeley.edu).

P. Ledochowitsch and M. M. Maharbiz are with the Berkeley Sensor and Actuator Center, University of California, Berkeley, Berkeley, CA 94720 USA (e-mail: ledochowitsch@berkeley.edu).

Color versions of one or more of the figures in this letter are available online at http://ieeexplore.ieee.org.

Digital Object Identifier 10.1109/LAWP.2013.2239252

Moreover, the regulated specific absorption rate (SAR) of electromagnetic (EM) energy into human body needs to be considered in the design of the on-body transmit antenna to guarantee human safety. At the frequencies considered, a conventional loop is not an optimal choice in terms of body SAR, and thus we chose to use a segmented loop [9].

For recording neural signals from the cortex, we have designed and fabricated an 8×8 electrode array with 400 μm electrode pitch that captures the scale of individual cortical columns. The array needed to conform to the cortex and was therefore fabricated at wafer level on a flexible and biocompatible polymer substrate, Parylene C, in a custom microelectromechanical systems (MEMS) process [10]. The total thickness of the conductive layer deposited by electron-beam evaporation was 200 nm (10 nm of Pt adhesion layer, 140 nm of ductile Au core, 50 nm of biocompatible Pt passivation). Minimizing device size and structural complexity was a top priority in the design. Therefore, the implant antenna is patterned onto the same substrate in the same process as the ECoG electrodes. For the frequency range of hundreds of megahertz to low-gigahertz range, this approach resulted in a conductor thickness of only a fraction of the skin depth. Therefore, additional loss due to current crowding was to be expected and, consequently, the degrees of freedom in the antenna design were greatly reduced. For instance, long and narrow antenna traces were to be avoided. Since a single-turn loop can efficiently extract energy from a magnetic field and enclose the electrode array to provide a single-layer structure with minimal surface area, we considered this configuration to be a fit choice for the application. The electrode array was modeled as a part of the antenna to account for the EM interaction between the two. Given the fixed size of the electrode array and the antenna design choices discussed in Section IV, the overall loop size is 6.5×6.5 mm^2.

The case study [9] of the 1×1-mm^2 implant loop showed that a combination of a transmitting loop with 15 mm inner diameter and a transmission frequency of 400 MHz maximized the link power efficiency across a transcranial link. However, at the given frequency, the loop carried a nonuniform current leading to hotspots in the near electric field, which led to increased body SAR. To alleviate this, the loop was segmented with series capacitors to force the current in phase. As shown by the results in Section IV, the same transmit antenna was also a fit choice for the BMI system considered in this work because the implant antenna is at the same depth and had the same rectangular loop configuration.

III. Characterization of the Wireless Link

The wireless link from the on-body transmitter to the implant was modeled as a linear two-port network characterized with Z-parameters. In this setting, the maximum obtainable power gain ($G_{\rm ma}$) and power gain of the network ($G_{\rm p}$) are [11]

$$G_{\rm ma} = \frac{P_{\rm rxa}}{P_{\rm txa}} = |z_{21}|^2 \cdot \left(2{\rm Re}(z_{11}){\rm Re}(z_{22}) - {\rm Re}(z_{12}z_{21}) + \sqrt{\left(2{\rm Re}(z_{11}){\rm Re}(z_{22}) - {\rm Re}(z_{12}z_{21})\right)^2 - |z_{12}z_{21}|^2}\right)^{-1} \quad (1a)$$

and

$$G_{\rm p} = \frac{P_{\rm ic}}{P_{\rm txa}} = \frac{|z_{21}|^2}{|z_{22}+Z_{\rm ic}|^2}\frac{{\rm Re}(Z_{\rm ic})}{{\rm Re}\left(z_{11} - \frac{z_{12}z_{21}}{z_{22}+Z_{\rm ic}}\right)} \quad (1b)$$

respectively. Here $P_{\rm txa}$ is the power delivered to the on-body transmit antenna, and $P_{\rm rxa}$ and $P_{\rm ic}$ are the power available from the implant antenna and the power delivered to the implant IC (impedance: $Z_{\rm ic}$), respectively. The difference between $G_{\rm ma}$ and $G_{\rm p}$ is that the latter includes the effect of possible impedance mismatch loss on the implant side. Importantly, for a wireless link, $G_{\rm ma}$ is the *link power efficiency*.

The implant antenna–IC power transfer efficiency ($0 < \tau \leq 1$), measuring the outcome of the impedance matching at this component interface, derived from (1), is

$$\tau = \frac{P_{\rm ic}}{P_{\rm rxa}} = \frac{G_{\rm p}}{G_{\rm ma}} \approx \frac{4{\rm Re}(z_{22}){\rm Re}(Z_{\rm ic})}{|z_{22}+Z_{\rm ic}|^2} \quad (2)$$

where the approximation holds for weakly coupled systems where $|z_{12}z_{21}|$ is small. In the studied BMI system, $|z_{12}z_{21}| < 0.5$, and the approximation in (2) held within 5% accuracy. Thus, we were confident to use the approximate expression of τ throughout the analysis presented below. This implied that the impedances of the on-body ($Z_{\rm txa}$) and implant ($Z_{\rm rxa}$) antennas were approximately independent of each other's terminations: $Z_{\rm txa} \approx z_{11}$ and $Z_{\rm rxa} \approx z_{22}$. Importantly, this enabled the new simple computational framework for the joint analysis of the power and voltage transfer to the implant IC as well as the evaluation of the impact of the variability in the IC impedance on the system performance.

The maximum transmit power of the system was limited by the maximum FCC-permitted body SAR (1.6 W/kg). In accordance with the above assumption of weak coupling, it was also reasonable to assume that the miniature implant antenna had a negligible impact on the SAR distribution of the transmit antenna near the surface of the body. With the maximum SAR-compliant transmit power ($P_{\rm txa,max}$), the corresponding power delivered to the implant IC was

$$P_{\rm ic} = \tau \cdot G_{\rm ma} \cdot P_{\rm txa,max}. \quad (3)$$

However, the operation of the system was not solely determined by the wireless link power transmission properties. In fact, the RF-to-dc conversion efficiency of the on-chip rectifier supplying the implant IC has nonlinear characteristics such that it drops rapidly at low RF voltages [6]. Thus, for the performance characterization, it is necessary to also compute the voltage ($V_{\rm ic}$) at the implant IC input.

To compute $V_{\rm ic}$, we analyzed the Thévenin equivalent circuit with the implant antenna acting as a generator loaded with the implant IC. In this setting, the power delivered to the implant IC is

$$P_{\rm ic} = \frac{1}{2}{\rm Re}(\widetilde{V}_{\rm ic}\widetilde{I}^*) = \frac{1}{2}{\rm Re}\left(\frac{V_{\rm ic}^2}{Z_{\rm ic}^*}\right) = \frac{R_{\rm ic}V^2}{2|z_{22}+Z_{\rm ic}|^2} \quad (4)$$

where tilde indicates complex phasor quantities and asterisk marks complex conjugates. Moreover

$$P_{\rm rxa} = \frac{P_{\rm ic}}{\tau} = \frac{V^2}{8{\rm Re}(z_{22})} \Rightarrow V_{\rm ic} = \sqrt{\frac{2|Z_{\rm ic}|^2}{{\rm Re}(Z_{\rm ic})}\tau G_{\rm ma}P_{\rm txa,max}} \quad (5)$$

where τ is the approximate implant antenna–IC power transfer efficiency given in (2).

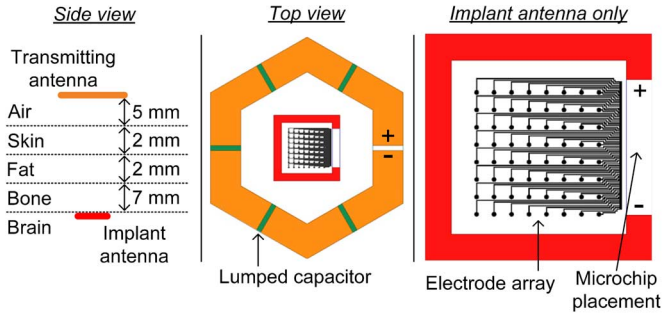

Fig. 2. Simulation model of the wireless link.

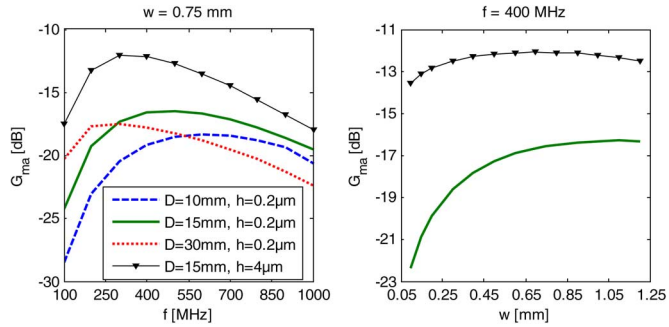

Fig. 3. Simulated link power efficiency for different antenna geometries.

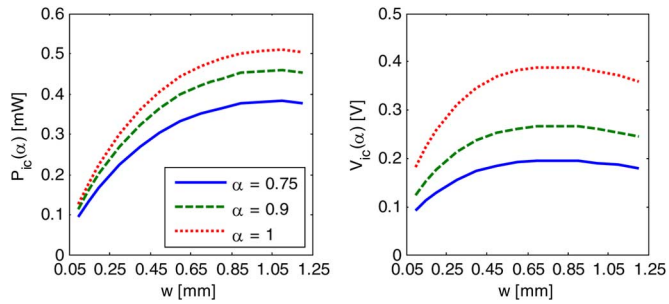

Fig. 4. Simulated $P_{\rm ic}$ at 400 MHz under different impedance-matching conditions and the corresponding lower bound of $V_{\rm ic}$.

For the purpose of uncertainty analysis it was important not only look at the power transfer but to also to compute V_{ic} in scenarios with various imperfect implant antenna terminations, which will affect the on-chip RF-to-DC conversion efficiency. In practice this may for instance occur due to IC fabrication variability and due to bandwidth limitations of the on-chip matching. Thus we considered a given antenna-IC matching tolerance: more than $\alpha \cdot 100\%$ of the available power from the implant antenna is being delivered to the IC. In another words, for a fixed α, we have $\tau \geq \alpha$. This is satisfied within a complex plane disk C_α with the center point and radius [12]

$$\left(\frac{2-\alpha}{\alpha}\mathrm{Re}(z_{22}), -\mathrm{Im}(z_{22})\right) \quad \text{and} \quad 2\mathrm{Re}(z_{22})\frac{\sqrt{1-\alpha}}{\alpha} \tag{6}$$

respectively, so that under the given matching tolerance the power delivered to the IC and the corresponding voltage at the IC input are greater than

$$P_{\rm ic}(\alpha) = \alpha \cdot G_{\rm ma} \cdot P_{\rm txa,max} \tag{7a}$$

and

$$V_{\rm ic}(\alpha) = \min_{Z_{\rm ic}\in C_\alpha} \sqrt{\frac{2|Z_{\rm ic}|^2}{\mathrm{Re}(Z_{\rm ic})}\tau G_{\rm ma} P_{\rm txa,max}} \tag{7b}$$

respectively.

Since the set C_α is fully characterized in terms of the system parameters, the minimum value of the previous expression is readily found with a numerical approach. Numerical results are provided in Section IV.

IV. Simulation Results

Simulations were conducted with ANSYS HFSS ver. 13, which is a full-wave EM field solver based on the finite element method. The simulation model is illustrated in Fig. 2. It consists of a layered tissue model with frequency-dependent dielectric properties given in [13], a segmented loop transmit antenna (see [9] for details), and the single-turn loop antenna enclosing the array of 64 electrodes. To account for additional loss sources, the equivalent series resistance of the segmenting lumped capacitors (50 mΩ) in the transmit antenna (see Fig. 2) and the implant antenna bonding resistance (0.3 Ω) were included in the simulation. The overall thickness of the Pt-Au-Pt (see Section II) conductor of the simulated and fabricated implant antenna is $h = 200$ nm. To gain insight into the impact of the current crowding in this sub-skin-depth conductor, simulations were also conducted with a single layer of gold with $h = 4$ μm (approximately one skin depth at 400 MHz).

The link power efficiency ($G_{\rm ma}$) was computed based on the simulated two-port Z-parameters using (1a). Fig. 3 shows the results for a wireless link composed of the 6.5×6.5-mm^2 implanted loop and segmented loop antennas (capacitors adapted at each frequency) with different inner diameters (D). The results on the left show that the $G_{\rm ma}$ exhibits a broad optimum and $D = 15$ mm maximizes $G_{\rm ma}$ in the 300–600-MHz band. Hence, further performance characterizations were done at 400 MHz. The results on the right justified the design choice for the implant antenna trace width (w). In fact, w has a major impact on $G_{\rm ma}$ due to the sub-skin-depth conductor: For $w < 0.5$ mm, $G_{\rm ma}$ dropped sharply, while exceeding $w = 0.75$ mm yielded little improvement. In comparison, the antenna with 4 μm conductor thickness achieved a 4-dB improvement in $G_{\rm ma}$ at 400 MHz. In this case, due to reduced current crowding, the trace width had little impact on $G_{\rm ma}$.

The power and voltage at the implant were further studied at 400 MHz using the $D = 15$ mm transmit antenna. Numerical modeling of the peak spatial-average body SAR was obtained using the SAR calculator based on [14] in HFSS. Following US FCC regulation, it was found that $P_{\rm txa,max} = 21$ mW at 400 MHz. Using this value and the simulated two-port Z-parameters, we obtained the results shown in Fig. 4. Recalling that the on-chip RF-to-dc conversion efficiencies drop when the voltage approaches the threshold voltage of the technology [6], in the studied scenario it may be best to choose $w = 0.75$ mm to maximize the voltage amplitude at the IC input—especially since this also provides close to maximal power delivery. In view of this, losing, e.g., 25% ($\alpha = 0.75$ in Fig. 4), of the

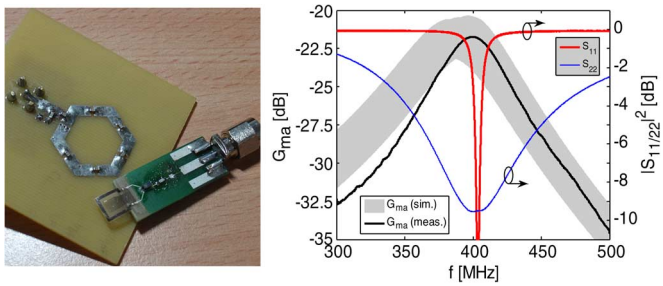

Fig. 5. Fabricated devices, the measured and simulated G_{ma} in air with the antenna separation of 2 cm, and the measured input reflection coefficients.

available power due to impedance mismatch may also drop the RF-to-dc conversion efficiency because the voltage swing was reduced as well.

V. Measurement Results

The results in Fig. 3 predicted that the current crowding in the thin implant conductor (5% of the skin depth at 400 MHz) to be a major loss mechanism affecting the system performance. Thus, we chose to attest the simulation model with link measurements in air.

The measurement was conducted as a two-port measurement with a vector network analyzer (VNA). The accuracy of a VNA is best around the characteristic impedance of 50 Ω. Thus, additional circuit board fixtures shown in Fig. 5 were implemented to impedance-match the designed antennas to 50 Ω. A surface-mount balun was incorporated in the implant antenna fixture to ensure a proper feeding mechanism for the miniature loop. The implant included the electrode array.

Fig. 5 presents the measured G_{ma} together with the results from additional simulations, where the feeding fixtures were included. In this experiment, the segmenting capacitors in the transmit antenna were adapted for 400 MHz. The variability of the capacitors (5% tolerance), the insertion loss of the balun (1–2.5 dB), and the implant antenna bonding resistance (0.3–1 Ω) were included in the model. The gray envelope illustrates the overall variability in G_{ma} due to the above sources of uncertainty. In addition, the measured input reflection coefficients are plotted on the right y-axis.

Near the matched frequency of 400 MHz, there was good agreement between the simulated and measured G_{ma}. The discrepancy, which emerged toward the lower frequencies, can be explained by the increased uncertainty in the VNA measurement due to the limited bandwidth of the transmit antenna: outside of the 370–450-MHz band, more than 98% of the input power was reflected back into the measurement instrument. In comparison, the measured implant antenna bandwidth appears broader due to the loss in the balun.

VI. Conclusion

The monolithic integration of an antenna with an ECoG electrode array on a thin film enables highly integrated implant architecture. Using full-wave EM simulations, we demonstrated how to optimize the operation frequency and antenna geometries to maximize link power efficiency while guaranteeing SAR compliance and sufficient voltage swing at the implant. The presented computational framework provides means for analyzing the sensitivity of the system performance toward the variability in the IC impedance. Measurements of the wireless link with the fabricated prototype antennas in air reinforce the validity of the antenna simulation model.

Future work will include experimental characterization of the wireless link performance in a realistic, biological environment and wireless testing with the antenna and electrodes bonded to an integrated circuit.

References

[1] M. A. Lebedev and M. A. L. Nicolelis, "Brain-machine interfaces: Past, present and future," *Trends Neurosci.*, vol. 29, no. 9, pp. 536–546, Sep. 2006.

[2] A. C. Koralek, J. D. Long, R. M. Costa, and J. M. Carmena, "Corticostriatal plasticity is necessary for learning intentional neuroprosthetic skills," *Nature*, vol. 483, no. 7389, pp. 331–335, Mar. 2012.

[3] G. Schalk and E. C. Leuthardt, "Brain-computer interfaces using electrocorticographic signals," *IEEE Rev. Biomed. Eng.*, vol. 4, no. 4, pp. 140–154, Apr. 2011.

[4] S. O'Driscoll, A. Poon, and T. H. Meng, "A mm-sized implantable power receiver with adaptive link compensation," in *Proc. ISSCC*, 2009, pp. 294–295.

[5] M. Mark, Y. Chen, C. Sutardja, C. Tang, S. Gowda, M. Wagner, D. Werthimer, and J. Rabaey, "A 1 mm^3 2 Mbps 330 fJ/b transponder for implanted neural sensors," in *Proc. VLSIC Symp.*, 2011, pp. 168–169.

[6] J. M. Rabaey, M. Mark, D. Chen, C. Sutardja, C. Tang, S. Gowda, M. Wagner, and D. Werthimer, "Powering and communicating with mm-size implants," in *Proc. Date Conf.*, 2011.

[7] Z. Xiao, C.-M. Tang, C. M. Dougherty, and R. Bashirullah, "A 20 μW neural recording tag with supply-current-modulated AFE in 0.13 μm CMOS," in *Proc. ISSCC*, 2010, pp. 122–123.

[8] H. N. Schwerdt, J. Chae, and F. A. Miranda, "Wireless performance of a fully passive neurorecording microsystem embedded in dispersive human head phantom," in *Proc. IEEE APS Symp.*, 2012.

[9] M. Mark, T. Björninen, L. Ukkonen, L. Sydänheimo, and J. Rabaey, "SAR reduction and link optimization for mm-size remotely powered wireless implants using segmented loop antennas," in *Proc. BioWireleSS Conf.*, 2011, pp. 7–10.

[10] P. Ledochowitsch, R. J. Félus, R. R. Gibboni, A. Miyakawa, S. Bao, and M. M. Maharbiz, "Fabrication and testing of a large area, high density, parylene MEMS μECoG array," in *Proc. MEMS Conf.*, 2011, pp. 1031–1034.

[11] R. S. Carson, *High-Frequency Amplifiers*. New York, NY, USA: Wiley, 1975.

[12] T. Björninen, A. Z. Elsherbeni, and L. Ukkonen, "Performance of single and double T-matched short dipole tag antennas for UHF RFID systems," *J. Appl. Comput. Electromagn. Soc.*, vol. 26, no. 12, pp. 953–962, Dec. 2011.

[13] S. Gabriel, R. W. Lau, and C. Gabriel, "The dielectric properties of biological tissues: III. Parametric models for the dielectric spectrum of tissues," *Phys. Med. Biol.*, vol. 41, no. 11, pp. 2271–2293, Nov. 1996.

[14] *IEEE Recommended Practice for Measurements and Computations of Radio Frequency Electromagnetic Fields With Respect to Human Exposure to Such Fields, 100 kHz–300 GHz*, IEEE Std C95.3-2002, 2002.